



An Expanded Model for the Pressure Effect in Metal Dusting of Mn-Containing Alloy 600 Based on Advanced Scale Characterization

M. C. Galetz¹ · C. Schlereth¹ · E. M. H. White¹ · T. Boll² · M. Bik³ · M. Sitarz³ · W.-T. Chen⁴ · B. Gleeson⁴

Received: 1 August 2023 / Revised: 21 September 2023 / Accepted: 22 September 2023 /
Published online: 25 October 2023
© The Author(s) 2023

Abstract

Commercial alloy 600 was exposed to a metal dusting inducing gas mixture to investigate the effect of ambient and elevated pressures on the oxide scale formation behavior. The formed scales on this alloy were investigated via Raman spectroscopy, transmission electron microscopy (TEM), and atom probe tomography (APT) to reveal the differences in their morphology and chemical composition(s). Raman spectroscopy revealed graphite within the chromia scales as well as oxide grains with Mn–Cr spinel. High-pressure exposure promoted the presence of Mn within the oxide scale, and APT demonstrated these Mn-enriched areas dissolved up to 4 at.% C. This was consistent with the TEM results, which confirmed higher amounts of Mn in the scale formed under elevated pressure, as well as crystalline graphite in the scales for both conditions. The consequences for the scale breakdown, reflecting the end of the incubation time for metal dusting attack, are discussed in light of these results. A two-fragment dissociative adsorption model for CO, previously applied to catalysis reactions, is proposed when Mn is incorporated into the chromia scale.

Keywords Metal dusting · Scale formation · Atom probe · Elevated total pressure

✉ M. C. Galetz
mathias.galetz@dechema.de

¹ DECHEMA-Forschungsinstitut, Theodor-Heuss-Allee 25, 60486 Frankfurt am Main, Germany

² Karlsruhe Institute of Technology (KIT) Institute of Nanotechnology,
Hermann-Von-Helmholtz-Platz 1, 76344 Eggenstein-Leopoldshafen, Germany

³ Faculty of Materials Science and Ceramics, AGH University of Science and Technology,
al. Mickiewicza 30, 30-059 Kraków, Poland

⁴ Department of Mechanical Engineering and Materials Science, University of Pittsburgh, 636
Benedum Hall, Pittsburgh, PA 15261, USA

Introduction

Metal dusting (MD) is a phenomenon that has long been known to degrade alloys at elevated temperatures in C-rich gases. C (e.g., from CO-containing gases) has a strong driving force for deposition and dissolution into the alloys, which subsequently induces disintegration of the metal into fine particles of graphite (after nucleation and growth) and metal powder. This poses a severe problem for industrial applications which use carbonaceous gases at high temperatures. The general underlying mechanisms and conditions have been very well elucidated through the extensive work of the groups of Grabke [1], Young [2], Szakálos [3], and Natesan [4], among others. Indeed, the seminal work of Prof. David Young and colleagues on metal dusting is succinctly discussed in Chapter 9 of his outstanding book *High-Temperature Oxidation and Corrosion of Metals*, 2nd Edition [5]. On the occasion of this special issue to commemorate Prof. Young's 80th birthday, the authors of this paper sincerely congratulate Prof. Young on the significant impact, he has made in the field of high-temperature corrosion research.

Metal dusting usually manifests in the form of localized pits after a certain incubation time of protective scaling. This time before scale breakdown depends on parameters such as alloy composition, gas environment, temperature, and pressure. The reasons and timeframe for the scale breakdown are still not well understood. For instance, chemical failure due to subsurface depletion, as well as mechanical failure of the scale, cannot readily explain the initiation of MD in highly alloyed Ni-based materials. Such materials are typically protected by an oxide scale, which grows at the relatively low O₂ partial pressures of the MD environment and forms a barrier against the high carbon activity of the gas and thus C transport into the alloy. Upon scale failure, MD in highly alloyed materials is caused by C diffusion into the subsurface zone, C oversaturation, and graphite formation [1–4]. Thus, the incubation time to pit formation strongly depends on the resistance of the oxide scale and therefore its chemical and mechanical integrity.

It has also been shown that an increase in total pressure lowers the incubation time and resistance to MD. This issue is industrially highly relevant since most industrial processes are typically performed above ambient pressure. Examples include H₂ and syngas plants or technologies such as autothermal reforming or dry reforming, in which methane and other hydrocarbons are reformed or partially oxidized to produce H₂ and CO [6]. Natesan and Zeng [4] demonstrated that the Ni-based alloy 602 CA is far more prone to develop MD at elevated pressures than at ambient pressure, with the same C activity in both gases. Additionally, they showed that if the gas composition remains the same, a higher pressure accelerates the attack. Both phenomena were confirmed to be generally valid for other alloys in the more current works of Madloch [7] and Rouaix-Vande Put [8], as well as Levi and Briggs [9].

An intuitive explanation to the above results may be offered by Le Chatelier's principle [10], where gases under pressure have a higher tendency to form solid reaction products, such as C. Additionally, the C activity is increased when a

gas is pressurized. However, the parameter “total pressure” is not really understood for MD and Le Chatelier’s principle, and activity is not sufficient to explain the reduced resistance of the oxide scale, as observed from shorter incubation times [8, 11]. Fundamental work was reported by Natesan and co-workers, who related the occurrence of MD to spinel oxide formation in the scale [12–14]. It was argued that the spinel should be reduced because chromia was much more resistant to MD. They suggested a model of a direct reaction of the C deposited on an oxidized metal surface, resulting in the reduction of spinel and formation of metallic Ni or Fe_3C . These phases are then thought to act as a continuous path for C transport through the oxide scale. On the other hand, Grabke et al. [15] showed that no C was dissolved in bulk spinel oxide when exposed to MD gas, and Röhner et al. [16] found that the incorporation of C into the scale takes place immediately upon initial exposure. These latter authors investigated the Fe–Ni–Cr-based alloy 800 after short exposure times and found small, highly disordered C clusters, in the range of 1–2 nm within the grain boundaries of the chromia scale that formed. If continuous, these C clusters [17] could allow for C ingress by bridging the scale. The formation of carbides underneath the oxide scale then becomes possible. Additionally, it was suggested that the C incorporated into the scale is aligned to the adjacent oxide crystals. The C uptake itself then might also induce oxide scale failure. For example, the pioneering work by D. Young and coworkers [13] used atom probe tomography to reveal C transport along the grain boundaries of a pre-formed chromia scale that was subsequently exposed to Ar-20CO_2 at 650 °C. All such findings describe pathways through the oxide scale. But the key questions that remain are (1) how C penetrates the oxide scale of highly alloyed materials after often very long incubation times, and (2) why the breakdown process is accelerated by an increased total pressure?

In the previous work, the difference in the incubation and attack of Ni-based alloy 600 at ambient and elevated pressures was described [18]. In the current work, the detailed underlying mechanisms are investigated that lead to scale failure and pit formation within a growing scale. At ambient pressure, a dense, continuous, adherent, and slow-growing chromia-rich scale typically formed on alloy 600 in the MD environment. On the other hand, the scale quickly developed sites of pit formation under elevated pressure. Relatively little information is available on the differences in the morphologies of scales grown in MD conditions. This can mainly be attributed to the difficulty in characterizing such thin scales (below 1 μm). Therefore, in this work, advanced characterization techniques with high spatial resolution and/or high surface sensitivity were employed to understand the effect of total pressure on the oxide scale formation and C uptake.

Experimental Procedures

The Ni-based alloy 600 was selected for the current study as one of the general use and relevance to the environments of interest. The composition of the alloy was measured by optical emission spectroscopy, and the results are presented in Table 1.

Table 1 Measured composition of alloy 600 (at.%)

Alloy	Ni	Cr	Fe	C	Mn	Si	Cu	Al	Ti	P	S
600	73.5	17.1	8.3	0.03	0.26	0.34	0.07	0.16	0.21	0.01	<0.001

Material was received from VDM Metals as a 5-mm-thick plate manufactured by hot-rolling and subsequent solution annealing. Prior to testing, samples were arc-wire cut to $10 \times 15 \times 5$ mm dimensions from the plate, and all surfaces were ground to a P1200-grit finish using SiC paper. The MD exposures were carried out by placing samples into alumina crucibles with slits for improved gas circulation. Exposures were conducted for 250 h at 620 °C under ambient pressure as well as at a total pressure of 18 bar (276 psi) [18]. The gas composition used was a mixture of H_2 -CO-CO₂-H₂O-CH₄ with a C activity in the syngas reaction, a_c , at 620 °C of 163 at 18 bar and of 9 at 1 bar. The gas flow rate within the furnace was set to 100 mL/min during the entirety of the test. More details can be found in [18]. The heating and cooling of the furnace was performed under argon (≤ 2 ppm O₂). Coke was removed by ultrasonication and cleaning with ethanol to obtain the net mass changes.

The samples were metallographically cut, cold mounted, and then polished after MD exposure. Initial characterization included optical microscopy, scanning electron microscopy (SEM), transmission electron microscopy (TEM), and Raman spectroscopy. Lift-outs for atom probe tomography (APT) were prepared with a focused ion beam from samples exposed under pressure (18 bar) and at ambient pressure (1 bar).

Results

Under ambient pressure, the alloy showed only minor weight gain and no MD attack after exposure for 250 h. By contrast, MD attack was already visible after 250 h for the elevated-pressure exposure in the form of pit formation and massive weight change. These findings were discussed in more detail in a previous publication [18].

Raman and SEM Investigation

Raman imaging, which has been shown to resolve the phase composition(s) of very thin multicomponent scales [19, 20], is included in Fig. 1 for the scales formed on the alloy 600 at the two pressures studied. The confocal image in Fig. 1a reveals a thin, homogeneous scale after exposure at 1 bar. After exposure at 18 bar, locally deeper attack was observed, especially along some grain boundaries, and the scale appears to be thicker. This is shown in Fig. 2. For the samples exposed under pressure, significant internal oxidation along grain boundaries can be seen, which is not present under ambient pressure.

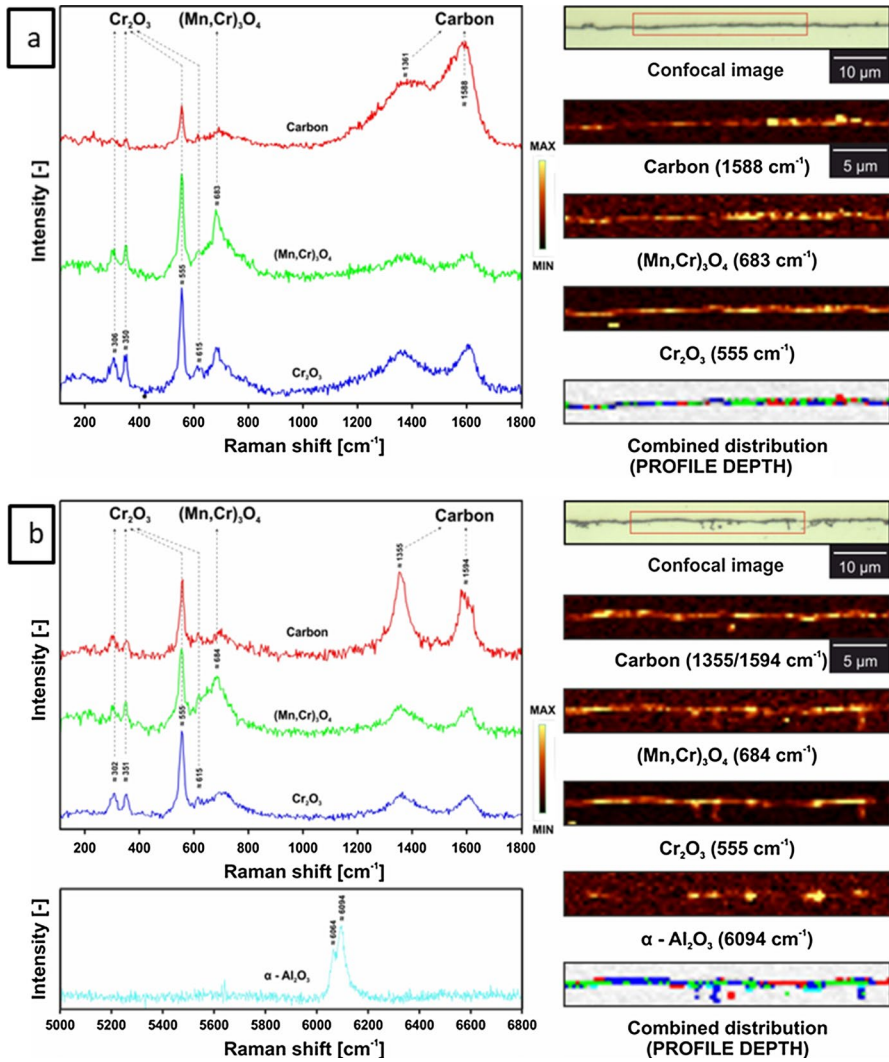


Fig. 1 Raman confocal imaging of alloy 600 exposed to an MD gas at 620 °C for 250 h at: **a** 1 bar and **b** 18 bar. The bands found are exemplified, and the corresponding distribution of phases is shown (based on the integration of the characteristic band with its Raman shift given in the brackets)

For both samples exposed at 1 and 18 bar, the scale is composed of three main components— Cr_2O_3 (assigned bands at ca. 555 cm^{-1} [21]), Mn–Cr spinel (attributed Raman modes at around 683 and 684 cm^{-1} [22, 23], respectively), and C. Additionally, for the sample exposed at 18 bar, an $\alpha\text{-Al}_2\text{O}_3$ signal was detected based on the occurrence of bands at ca. 6064 and 6094 cm^{-1} . The corresponding vibrations vary from the typical data that are found in the literature for alumina (bands at 1370 and 1400 cm^{-1} for 633 nm laser line [24, 25]), but such bands can also be attributed to luminescence caused by impurities in Al_2O_3 [26].

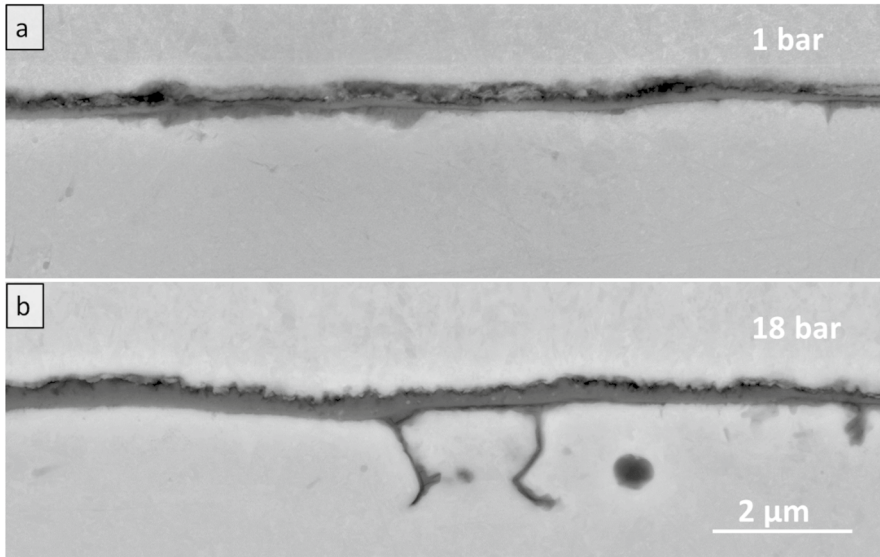


Fig. 2 SEM images of the oxide scales and the subscale regions of alloy 600 exposed to an MD gas at 620 °C for 250 h at: **a** 1 bar and **b** 18 bar (above the oxide scale, the electroplated Ni layer from metallographic preparation is visible)

Quantitatively, Cr_2O_3 is the dominant constituent within the scale based on the intensities of the characteristic bands as well as the distribution maps. Nevertheless, for both pressures, Mn–Cr spinel was found within the scales. The signal distribution of the spinel seems to be mixed with the chromia in both cases. For the high-pressure sample, both oxides can also be found in the areas of local internal attack along the grain boundaries. The distribution maps of $\alpha\text{-Al}_2\text{O}_3$ suggest that it formed locally under the Cr-rich scale.

Distinctive differences can be observed between the scales from the modes assigned to C and the Cr_2O_3 /spinel intensity ratios due to the change in pressure. Even though the C positions of the typical D and G bands [27, 28] do not differ a lot ($\sim 6\text{ cm}^{-1}$ for both), the spectra shape do. For the exposure at 1 bar, the spectrum is very similar to those observed for materials described as diamond-like C (dlc), i.e., in [27, 29]. Whereas, for the higher-pressure sample, the different shapes of the spectrum (easily distinguishable D and G bands, as well as lack of an additional band ascribed to amorphous C ($\alpha\text{-C}$) (at ca. 1510 cm^{-1} [27]) that is present for the sample exposed at 1 bar) indicate the occurrence of more crystalline graphite, similar to C nanotubes (CNTs) [30, 31].

TEM Investigation

A higher resolution, but also significantly more local, TEM analysis of the scales of alloy 600 is included in Fig. 3a and b for the samples exposed at ambient and

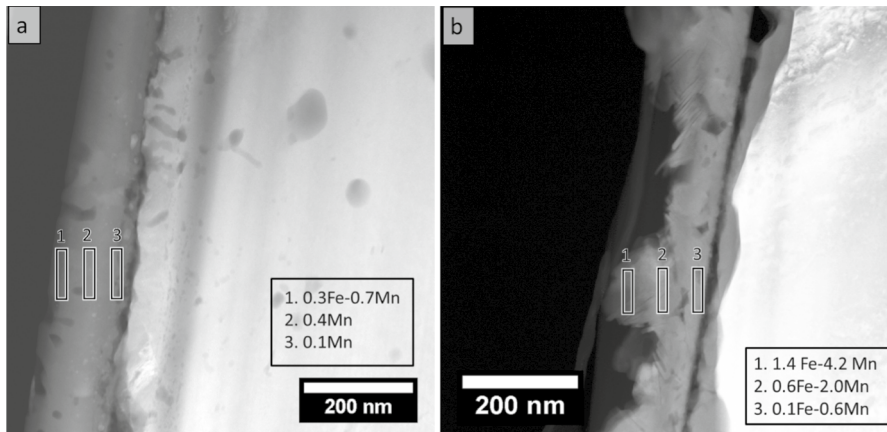


Fig. 3 STEM HAADF images of alloy 600 oxide scales exposed to an MD gas at **a** 1 and **b** 18 bar at 620 °C for 250 h with EDS area measurements for Fe and Mn contents (values given in at.%)

elevated pressures, respectively. Confirming the SEM and Raman results, a smoother and more homogeneous scale was formed under the ambient-pressure conditions. Additionally, chemical differences in the oxide scales were revealed using EDS analysis. Both alloys mainly form a Cr-rich scale as an outer oxide, but the oxide scales also contain Fe and Mn for both pressures. Within the investigated part of the scale, higher levels of these elements were present for the 18 bar sample compared to the ambient exposure. In Fig. 3, the contents of such elements are given, and the respective averaged windows of measurement for the different scales are shown. Interestingly, especially near the gas/oxide interface, the amounts of Fe and Mn are about 4–6 times higher at 18 bar than at ambient pressure. Additional distinct features of the scale grown at high pressure are the presence of internal oxidation of Al and Si. Such findings confirm the results from the Raman measurements regarding the presence of alumina, which also only occurred for the sample exposed under pressure.

For the pressurized sample, more C was also found in the scale. This graphite morphology and distribution is more closely assessed in Figs. 4 and 5. Two line scans at different locations show that the oxide (represented by O and Cr) and graphite are adjacent. While the total content of C cannot be quantitatively determined in a reliable way by EDS, the transition from chromia to graphite is obvious. In Fig. 5, another location within the scale is shown that again confirms the presence of the graphite layers in the outer part of the scale and suggests a certain orientation relationship between chromia and graphite. Figure 5b indicates that the graphite grew adjacent to the $[1\bar{1}02]$ growth direction of chromia. For improved illustration, several Cr atoms within the crystal lattice are included in Fig. 5b.

Atom Probe Analysis

To further investigate the composition of the oxide scales, Figs. 6 and 7 present atom probe tomography results of the alloy 600 oxide scales from tips prepared after

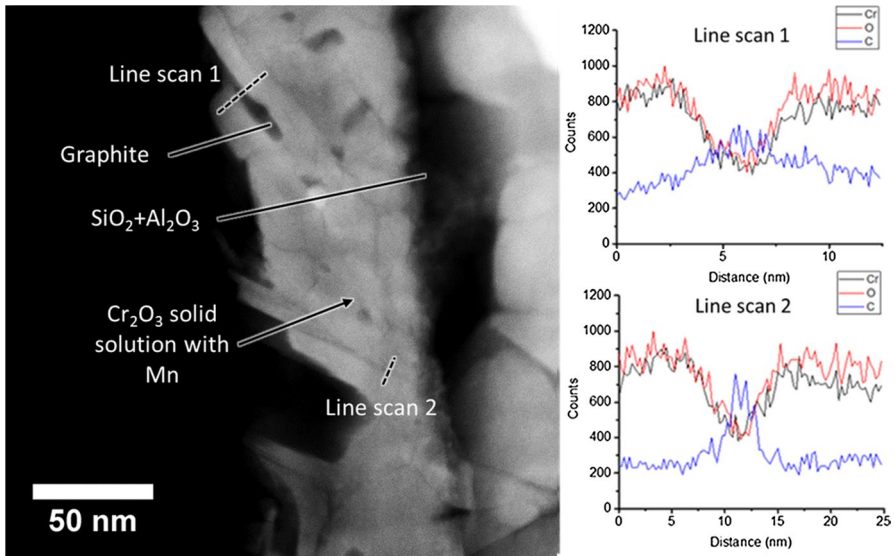


Fig. 4 Higher magnification STEM HAADF image of the alloy 600 oxide scale formed at elevated pressure under MD gas exposure at 18 bar, 620 °C for 250 h (also shown in Fig. 5) with line scans of C, O, and Cr concentrations along the indicated dashed lines

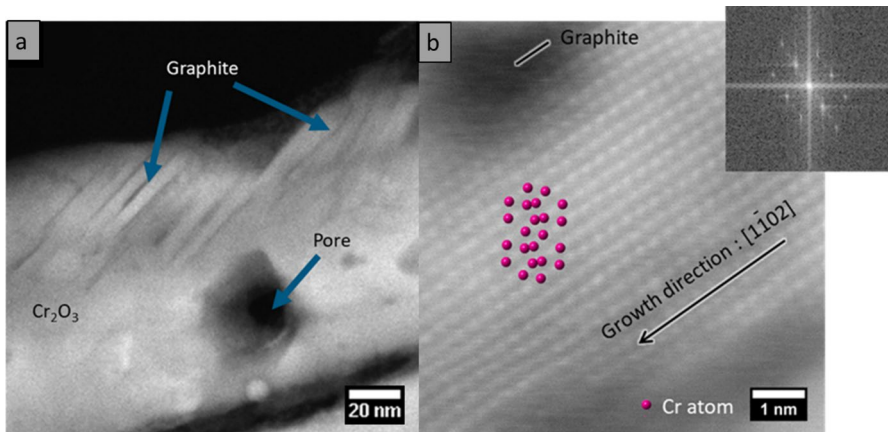


Fig. 5 **a** Highest magnification STEM HAADF image of the alloy 600 oxide scale grown under pressure with MD gas exposure at 18 bar, 620 °C for 250 h and **b** the determined crystal orientation relationship between chromia and graphite (Inset shows the corresponding selected area (electron) diffraction image)

exposure. In Figs. 6a and 7a, an overview of the element distributions in two representative tips is shown for scales that were grown at 1 bar and 18 bar, respectively. In Figs. 6b and 7b, only the oxide is shown. Traces of Cu (<0.14 at.%) and Ar or Ca (<0.03 at.%) were also found in the oxide but are not shown. Fe is only shown in the image of the oxide, since in the overview images in Figs. 6a and 7a, Fe had the same

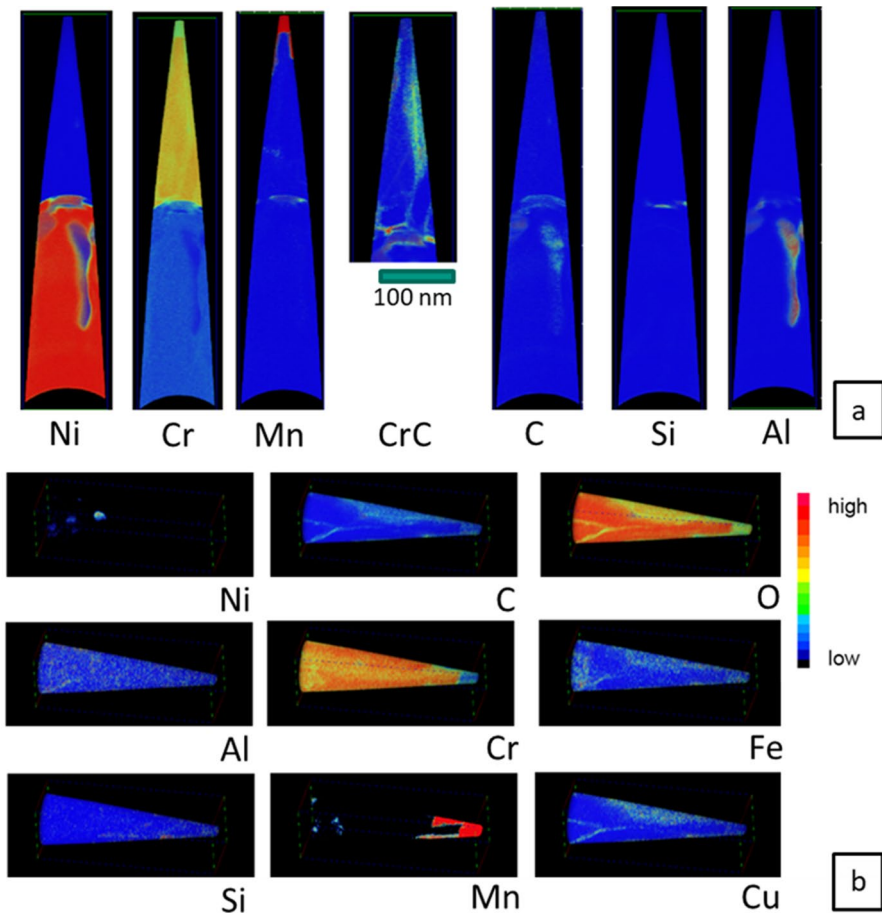


Fig. 6 Three-dimensional reconstruction of the oxide scale grown on alloy 600 at ambient pressure (1 bar), 620 °C for 250 h: **a** Overview of the tip (scale–gas interface on the top) including the interface to the substrate and **b** more detailed view of the top section of the tip (scale–gas interface to the right)

distribution as Ni. The Ni signal intensity can be used to clearly distinguish between the oxide and the metal matrix. The APT of such tips confirmed again that the oxide scales mainly consist of a Cr_2O_3 -rich layer.

Additionally, Mn oxide was found locally in the investigated tips. For the tip exposed at ambient pressure, Mn oxide was only present at the very surface/top of the tip, while in the high-pressure sample, larger areas of the Mn-rich oxide were found. In all such areas, except for the very surface of the scale in contact with the gas, Mn was accompanied by 3–4 at.% C, as indicated in the distribution maps. For the scale grown at 1 bar, a very low C signal was present at the grain boundaries. Grain boundaries were decorated more strongly with C at higher pressure, and within both the 1 and 18 bar oxide scales, Fe was found in small amounts up to 0.4 at.% in the Cr- and O-rich regions. Such low amounts confirmed the Raman findings that Cr–Fe spinels are not present.

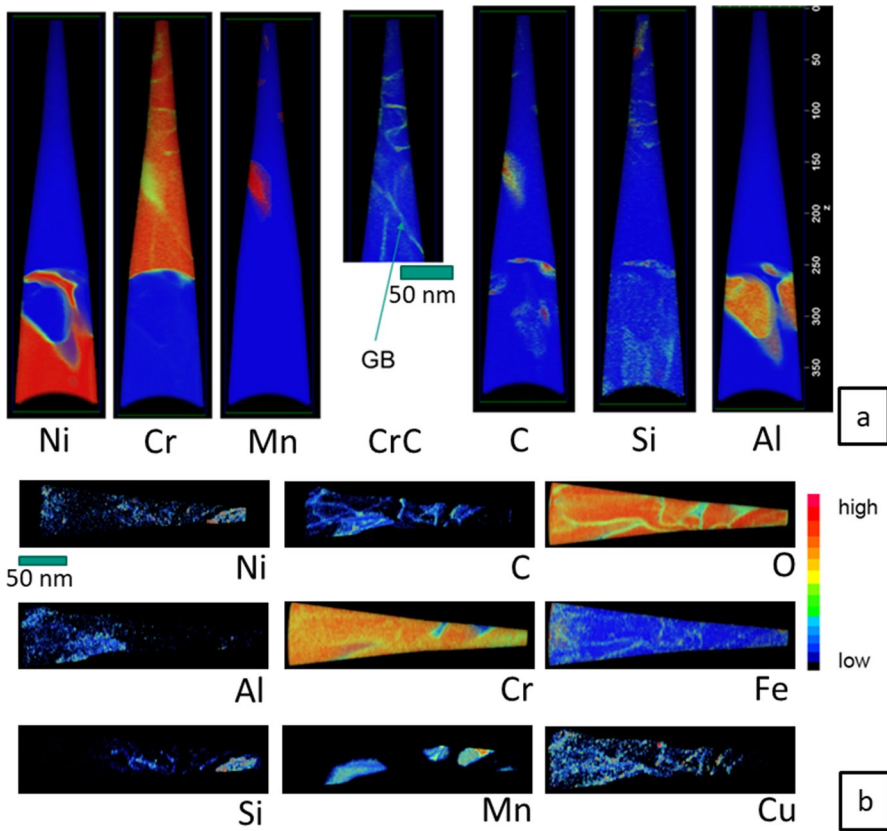


Fig. 7 Three-dimensional reconstruction of the alloy 600 oxide scale grown at elevated pressure (18 bar), 620 °C for 250 h: **a** Overview of the tip (gas–scale interface at the top) including the interface to the substrate and **b** more detailed view of the top end of the tip (gas–scale interface to the right)

For the lower magnification images (Figs. 6a and 7a), two C signals are given, one from C only and one from CrC, which was mainly observed at the grain boundaries, especially at higher pressure. Outside of the chromia, however, C is difficult to distinguish from O (or S) since the atomic mass of CrC is equal to the atomic mass of two O₂ molecules, and thus can overlap and be convoluted in the atom probe measurement. Nevertheless, a comparison of the isotope distribution enables attributing the majority of the peak to CrC in the chromia part of the measurement.

Discussion

Investigation of the influence of total pressure on the oxide scale formation on alloy 600 in MD conditions showed that the scale grew slightly thicker at higher pressure. The Cr–Mn spinel was identified for both exposures using the Raman

measurements; however based on the TEM and APT results, higher amounts of Fe, Mn, and C are also present in the chromia scales exposed at higher pressure. This is especially true for Mn, which was found in much higher concentrations in the TEM-EDS assessments, as well as in the atom probe measurements of the scales grown at elevated pressure. The alumina measured at the interface with the substrate could also only be detected in the sample exposed at the higher pressure and can decrease the scale growth, which interestingly was slightly higher for the sample exposed at higher pressure.

The limited past studies on the effect of elevated pressures on scaling kinetics do not show a clear trend. For pure Ni, Baur and Bartlett [32] found that in oxygen above 1000 °C, the oxidation rate is insensitive to pressure above atmospheric, while, in a study on a Ni-based superalloy, Reynolds et al. [34] found a thicker oxide layer on samples exposed in air at 650 °C and 1 bar pressure compared with others exposed at 40 bar. They also reported a change in the predominant oxide from Cr_2O_3 at ambient pressure to a $(\text{Ni},\text{Co})\text{Cr}_2\text{O}_4$ spinel at higher pressure, that, in contrast with their results, one would expect to grow faster and not slower. On the other hand, similar to the results here, under supercritical CO_2 atmospheres, Pint et al. [33] found that for alloy 625, the scale at 30 MPa was slightly thicker when compared to the exposures at 0.1 MPa in sCO_2 and even in laboratory air. Further investigation of the influence of total pressure on scale growth kinetics and associated phase constitution is necessary to determine whether pressure is changing the transient, steady state, or both behaviors.

With respect to MD resistance, neither the alumina at the interface, nor the incorporation of Mn into chromia, can easily explain the scale breakdown after only 250 h under higher pressure, when compared to an intact oxide scale (no pits) at ambient pressure. Chromia scales are among the most effective, slow-growing oxide barriers and are protective for much longer at much higher temperatures than 620 °C before chemical failure occurs. Even in air, the presence of Mn is not reported to have a significant detrimental impact on the properties of chromia, e.g., [35]. However, as discussed in the introduction, this might change with C uptake, which is among the secondary oxidants that are known to penetrate scales and lower protective properties. The Mn-rich oxide had up to 4 at.% C concentration in the APT measurements. The Raman measurements suggest that the crystallinity, and thus morphology, of the C present within the scale also changes with pressure, and increased total pressure increases scale susceptibility to C uptake. This is consistent with a recent XPS study on alloy 601 [36] and is also proven by the graphite striations in the TEM investigations and the graphite signal of the APT measurements. These suggest that C is present in much higher amounts at the grain boundaries at increased pressure. On the other hand, the grain boundary C that is already picked up during incubation might explain the slightly higher thickness of the scale after the exposure under pressure. Chromia should grow solely by grain boundary diffusion at the low temperature of this study, and the presence of C along the grain boundaries could influence the Cr diffusion and thus scale growth. Another factor that may have impacted the scaling behavior, and which may be related to the presence of C in the grain boundaries of the scale, is the stronger internal oxidation of stable oxide formers and

internal grain boundary oxidation, which was also much more pronounced at the elevated pressure.

However, besides the C at the grain boundaries, the presence of other C clusters in the scales formed at the elevated pressure is interesting. As shown in Fig. 5, a preferential graphite orientation to the chromia scale suggests that the graphite nucleation and growth are related to the orientation of the oxide, and thus could be responsible for scale failure. This finding, along with the increased C content in the Mn-rich oxide, suggests that the structure and scale morphology play a significant role in the C uptake and the incubation and growth behavior of graphite within chromia scales in MD environments.

The structure and morphology of a chromia scale is closely tied to its defect structure. It has long been discussed that chromia exhibits semiconductor properties depending on the O_2 partial pressure. Intrinsic electronic conductor behavior of chromia was described by Crawford and Vest in 1964 [37] and during the 90s by Kofstad's studies [38, 39]. Su and Simkovich [40] suggested that for low $p(O_2)$ n -type semiconductor behavior prevails, which is in agreement with the more recent work from Latu-Romain et al. [41] who found that below 800 °C chromia grown at low $p(O_2)$ is always O-deficient n -type. These findings are important for the current study because of the difference in O vacancy concentrations, which can be considered as point defects in the growing scale (with V^{**} vacancies being predominant in n -type chromia). Considering the observed Mn (or Fe) cations with a M^{2+} charge substituting Cr^{3+} cations to a certain degree in the scale, the prevalence of O^{2-} vacancies must be even higher to balance the doping charge.

Two phenomena are thus inferred to play a crucial role in the breakdown of the oxide scales: (1) C uptake through graphite nucleation and growth with a crystallographic orientation relationship to chromia and (2) increased Mn (and Fe) within the chromia scale leading to a higher defect concentration and catalytic activity for gas decomposition. The observed C ingress was aligned with the chromia grain orientation but also C was found in the areas with higher Mn content. The comparison to catalytic studies is interesting, since it is known that CO_2 adsorbs and decomposes easily and completely on O-deficient magnetite [42, 43]. The high reactivity for carbonaceous gases along with their reduction to C is assigned to the reactive sites where an electron is readily donated to the C (from Mn^{2+} or Fe^{2+}), and the O from the gas molecule is incorporated into a lattice site in the form of O^{2-} . This model, illustrated in Fig. 8 as a two-fragment dissociative adsorption model for CO (adjusted from the three-fragment adsorption model for CO_2 from [42]), can explain the higher uptake of C into the scales that include Mn or Fe. This model is also in accordance with the study of Natesan et al. [4], who showed that the Fe to Cr ratio in the spinel has a strong impact on the weight gain in MD. Such uptake into the spinel, and later transport along graphite precipitates in the scale, is suggested as a major mechanism that can lead to scale failure and thus pit initiation. It should be noted that the suggested formation of metallic particles [12] by the reduction of Ni-rich spinels within the oxide scale is an alternative mechanism to end incubation and is neither supported nor excluded by the current study; however, such particles were not found for alloy 600.

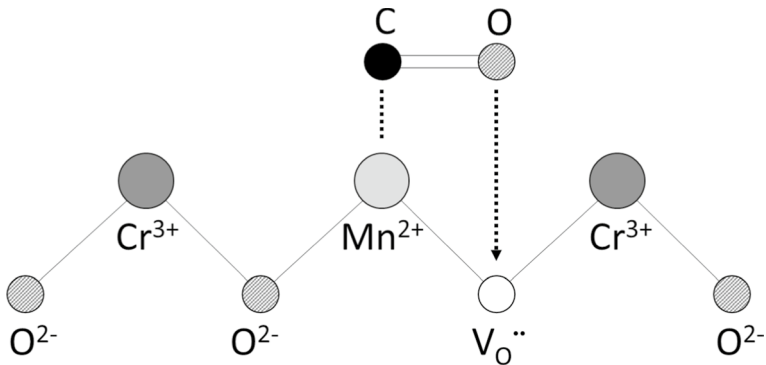


Fig. 8 Illustration of the suggested interaction between CO and the adsorption site on the surface of O^{2-} -deficient magnetite according to the two-fragment dissociative adsorption model

Finally, when it comes to the influence of elevated total pressure, adsorption processes are accelerated by an increased overall pressure until reaching a certain threshold [44]. Additionally, as proven by the different analytical methods, the scales grown at high pressure contain more additional elements (Mn and Fe) alongside Cr. This may be due to the high pressure affecting the initial transient stage of oxidation, and further testing and analysis would be needed for validation. Regardless, both processes, either individually or together, offer valid reasons for the faster scale failure that was observed for the elevated gas pressure exposures.

Summary

The scales formed on alloy 600 in an MD environment under ambient and elevated pressures were investigated with two main findings. First, a higher amount of Mn was observed in the scales grown under pressure with C located in the areas with higher Mn content. Second, C precipitates were found in the scale grown under pressure, and ingress was aligned with the chromia grain orientation. A dissociative adsorption model of CO into the Mn-/Fe-rich spinel or doped chromia is suggested that can explain the C uptake and later precipitation of graphite within the scale. This model also helps to explain why this mechanism is accelerated at elevated pressures.

Acknowledgements This work has received funding from the European Union's Horizon 2020 research and innovation program under Grant Agreement No. 958192. The authors would like to thank Mathias Röhrig and Melanie Thalheimer for helping with the exposure test and SEM work, respectively.

Author contributions MG wrote the draft of the manuscript with strong support from EW, CS, MB, and BG in the design of the work and interpretation of data. TB, MB, and WTC mainly contributed in data acquisition and analysis with APT, Raman, and TEM, respectively. All authors reviewed the manuscript critically and contributed to the interpretation of data.

Funding Open Access funding enabled and organized by Projekt DEAL.

Declarations

Conflict of interest The authors declare no competing interests.

Open Access This article is licensed under a Creative Commons Attribution 4.0 International License, which permits use, sharing, adaptation, distribution and reproduction in any medium or format, as long as you give appropriate credit to the original author(s) and the source, provide a link to the Creative Commons licence, and indicate if changes were made. The images or other third party material in this article are included in the article's Creative Commons licence, unless indicated otherwise in a credit line to the material. If material is not included in the article's Creative Commons licence and your intended use is not permitted by statutory regulation or exceeds the permitted use, you will need to obtain permission directly from the copyright holder. To view a copy of this licence, visit <http://creativecommons.org/licenses/by/4.0/>.

References

1. H. J. Grabke, *Werkstoffe und Korrosion* **54**, 736 (2003).
2. D. J. Young and J. Zhang, *JOM* **64**, 1461 (2012).
3. P. Szakalos, *Materials Science Forum* **552–523**, 571 (2006).
4. K. Natesan and Z. Zeng, *Development of Materials Resistant to Metal Dusting Degradation*. U.S. Department of Energy (2006).
5. D. J. Young (ed.), *High temperature oxidation and corrosion of metals*, (Elsevier, Amsterdam, 2016).
6. F. Giroudière, J. L. Ambrosino, B. Fischer, D. Pavone, E. Sanz-Garcia, A. Le Gall, E. Soutif, and H. Vleeming, *Oil & Gas Science and Technology-Revue d'IFP Energies Nouvelles* **65**, 673 (2010).
7. S. Madloch, *Effect of Pressure on Metal Dusting and the Protection of Affected Materials by Oxide Forming and Catalytically Inhibiting Diffusion Coatings*, (Shaker Verlag, Aachen, 2018).
8. A. Rouaix-Vande Put, A. Fabas, S. Doublet, and D. Monceau, *Oxidation of Metals* **87**, 655 (2017).
9. T. P. Levi, N. Briggs, I. E. Minchington, and C. W. Thomas, *Werkstoffe und Korrosion* **53**, 239 (2002).
10. P. Atkins and J. de Paula, *Physikalische Chemie*, (Wiley-VCH, Weinheim, 2006).
11. C. Schlereth, K. Hack, and M. C. Galetz, *Corrosion Science* **206**, 110483 (2022).
12. Z. Zeng, K. Natesan, Z. Cai, and S. B. Darling, *Nature Materials* **7**, 641 (2008).
13. Z. Zeng, K. Natesan, and M. Grimsditch, *Corrosion* **60**, 6323 (2004).
14. Z. Zeng and K. Natesan, *Oxidation of Metals* **66**, 1 (2006).
15. I. Wolf and H. J. Grabke, *Solid State Communications* **54**, 5 (1985).
16. D. Röhnert, M. Schütze, and T. Weber, Performance of several nickel base alloys in metal dusting atmospheres, in *Corrosion 2007 Conference & Expo* (NACE, Nashville 2007).
17. A. Agüero, M. Gutiérrez, L. Korcakova, T. Nguyen, B. Hinnemann, and S. Saadi, *Oxidation of Metals* **76**, 23 (2011).
18. S. Madloch, A. Soleimani-Dorcheh, and M. C. Galetz, *Oxidation of Metals* **89**, 483 (2018).
19. Ł. Mazur, J. Ignaczak, M. Bik, S. Molin, M. Sitarz, A. Gil, and T. Brylewski, *Journal of Hydrogen Energy* **47**, 6295 (2022).
20. M. Bik, M. Galetz, J. Dąbrowa, K. Mroccka, P. Zając, A. Gil, P. Jeleń, M. Gawęda, M. Owińska, M. Stygar, and M. Zajusz, *Applied Surface Science* **576**, 151826 (2022).
21. R. L. Farrow, R. E. Benner, A. S. Nagelberg, and P. L. Mattern, *Thin Solid Films* **73**, 353 (1980).
22. Y. Chen, Z. Liu, S. P. Ringer, Z. Tong, X. Cui, and Y. Chen, *Crystal Growth & Design* **7**, 2279 (2007).
23. B. D. Hosterman, *Raman Spectroscopic Study of Solid Solution Spinel Oxides* (2011).
24. S. Hakkar, S. Achache, F. Sanchette, Z. Mekhalif, N. Kamoun, and A. Boumaza, *Journal of Molecular and Engineering Materials* **7**, 1950003 (2019).
25. C. Boulesteix, V. Kolarik, and F. Pedraza, *Corrosion Science* **144**, 328 (2018).

26. A. B. Kulinkin, S. P. Feofilov, and R. I. Zakharchenya, *Physics of the Solid State* **42**, 857 (2000).
27. A. C. Ferrari and J. Robertson, *PRB* **61**, 14095 (2000).
28. M. Bik, J. Szewczyk, P. Jeleń, E. Długoń, W. Simka, M. Sowa, J. Tyczkowski, J. Balcerzak, E. Bik, K. Mrocza, and M. Leśniak, *Electrochimica Acta* **309**, 44 (2019).
29. A. C. Ferrari and J. Robertson, *Philosophical Transactions of the Royal Society of London. Series A: Mathematical, Physical and Engineering Sciences* **362**, 2477 (2004).
30. E. Długoń, W. Niemiec, A. Frączek-Szczypta, P. Jeleń, M. Sitarz, and M. Błażewicz, *Spectrochimica Acta A Molecular and Biomolecular Spectroscopy* **133**, 872 (2014).
31. M. Zambrzycki, P. Jeleń, and A. Frączek-Szczypta, *Journal of Materials Science* **57**, 9334 (2022).
32. J. P. Baur, R. W. Bartlett, J. N. Ong, and W. M. Fassell, *Journal of the Electrochemical Society* **110**, 185 (1963).
33. B. A. Pint and K. A. Unocic, *JOM* **70**, 1511 (2018).
34. T. D. Reynolds, M. P. Taylor, D. J. Child, and H. E. Evans, *Materials at High Temperatures* **35**, 130 (2018).
35. L. Niewolak, D. J. Young, H. Hattendorf, L. Singheiser, and W. J. Quadackers, *High Temperature Corrosion of Materials* **82**, 123 (2014).
36. C. Schlereth, M. Weiser, E. M. H. White, P. Felfer, and M. Galetz, *Journal of Materials Science*.
37. J. A. Crawford and R. W. Vest, *Journal of Applied Physics* **35**, 2413 (1964).
38. A. Holt and P. Kofstad, *Solid State Ionics* **69**, 137 (1994).
39. A. Holt and P. Kofstad, *Solid State Ionics* **117**, 21 (1999).
40. M.-Y. Su and G. Simkovich, *Non-Stoichiometric Compounds: Surfaces, Grain Boundaries and Structural Defects, NATO ASI Series, Series C*, Vol. 276. (Springer, Dordrecht, 1989).
41. L. Latu-Romain, Y. Parsa, S. Mathieu, M. Vilasi, M. Ollivier, A. Galerie, and Y. Wouters, *Oxidation of Metals* **86**, 497 (2016).
42. K. Nishizawa, T. Kodama, M. Tabata, T. Yoshida, M. Tsuji, and Y. Tamaura, *Faraday Transactions* **88**, 2771 (1992).
43. K. Akanuma, K. Nishizawa, T. Kodama, M. Tabata, K. Mimori, T. Yoshida, M. Tsuji, and Y. Tamaura, *Journal of Materials Science* **28**, 860 (1993).
44. S. Azizian and S. Eris, in *Interface Science and Technology*, ed. M. Ghaedi (Elsevier, 2021), p. 445.

Publisher's Note Springer Nature remains neutral with regard to jurisdictional claims in published maps and institutional affiliations.